CHEMISTRY OF MATERIALS

pubs.acs.org/cm

Article

Regulating the Alloying Degree and Electronic Structure of Pt−Au Nanoparticles for High-Efficiency Direct C_{2+} Alcohol Fuel Cells

Minghang Jiang, Yi Hu, Wenjun Zhang, Lei Wang, Songyuan Yang, Junchuan Liang, Zewen Zhang, Xiaoli Zhang, and Zhong Jin*

Cite This: *Chem. Mater.* 2021, 33, 3767−3778

Read Online

ACCESS | Metrics & More | Article Recommendations | Supporting Information

ABSTRACT: Direct alcohol fuel cells represent a promising green and sustainable route for chemical to electrical energy conversion; however, designing highly efficient electrocatalysts for the electro-oxidation of C_{2+} alcohol molecules is an ongoing challenge. Herein, we report a convenient room-temperature reduction method to fabricate a series of Pt−Au alloy catalysts with controllably tailored alloying degrees and particle diameters (4.6−7.9 nm) for enhancing the electro-oxidation capability toward C_{2+} alcohols. Benefiting from the strong electron interactions between Pt and Au, the electronic state and size of the alloy nanoparticles can be effectively optimized, alleviating the CO poisoning and aggregation problem of the catalytic species. As a result, the $Pt_{45}Au_{55}$ alloy nanoparticles grown in situ on carbon nanotubes ($Pt_{45}Au_{55}$/CNTs) show an enhanced C−C bond cleavage ability, as confirmed by a quantitative analysis of the final C_2 oxidation products as well as by comparing the oxidation activity in different C_1−C_3 alcohols and other high-energy-density molecules. The $Pt_{45}Au_{55}$/CNTs catalyst exhibits excellent catalytic activity (1746 $mA{\cdot}mg_{Pt}^{-1}$), high CO tolerance, and good stability for the ethanol oxidation reaction (EOR) in an acidic medium. Moreover, the $Pt_{38}Au_{62}$/CNTs catalyst displays dramatically enhanced ethanol oxidation activity (13 993 $mA{\cdot}mg_{Pt+Au}^{-1}$) in an alkaline medium. The proposed rational design of Pt−Au alloy catalysts with controllable alloying degrees and particle sizes provides a feasible strategy for boosting the overall performance of Pt-based electrocatalysts for the direct C_{2+} alcohol fuel cells.

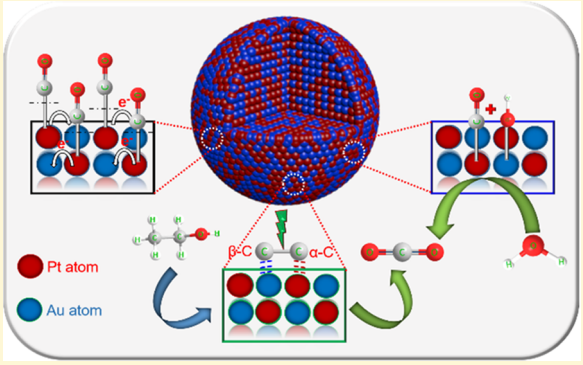

INTRODUCTION

Over the past years, direct alcohol fuel cells have been increasingly studied as an alternative power source to address increasing global energy and environmental problems, due to their higher energy density, low toxicity, safe storability, and renewability of alcohol molecules, especially ethanol.[1,2] To date, platinum-based electrocatalysts are still the most active materials for the ethanol oxidation reaction (EOR) compared with Pt-free catalysts under acidic conditions.[3] However, monometallic Pt surfaces are easily adsorbed by CO-like poisoning intermediates (CO_{ads}), thereby impeding the EOR.[4,5] It is generally considered that the EOR follows a dual-path reaction process in acidic medium via the C_1 and C_2 pathways. For instance, the complete ethanol oxidation to CO_2, producing 12 electrons through the splitting of the C−C bond (C_1 pathway), is significantly suppressed, whereas the incomplete oxidation of ethanol prevails during the EOR, generating CH_3COOH and CH_3CHO (C_2 pathway).[1,6−8] In other words, the complete electro-oxidation of C_{2+} alcohol molecules to CO_2 requires a thorough cleavage of C−C bonds, which is still a challenge even for pure Pt catalysts. Therefore, improving the C−C bond cleavage capability and CO tolerance of Pt-based catalysts is a promising route to boost the electrocatalytic performances for the electro-oxidation of C_{2+} alcohols.

It has been reported that CO molecules can donate their 5σ-orbital electrons to the unoccupied d-orbitals of Pt to form σ bonds.[9−16] When Pt is enriched with excessive negative charges, it will feed electrons back to the antibonding 2π* orbitals of adsorbed CO to form feedback π bonds. After that, a σ−π bond with strong adsorption is formed between CO_{ads} and the Pt active site. Therefore, pure Pt-based catalysts are prone to CO poisoning during alcohol electro-oxidation processes. Notably, Pt−M alloy catalysts (M = Cu,[12] Ru,[5] Sn,[15] Rh,[1] Bi,[16] and so on) can adjust the outer electronic structure of Pt and shift the d-band center of Pt down, thereby weakening the feedback π bond between Pt and CO; this shift is beneficial for regaining the Pt active sites by the electronic effect.[9,11] Additionally, the incorporated non-platinum metal is

Received: March 12, 2021
Revised: April 20, 2021
Published: May 5, 2021

conducive to the activation and dissociation of H_2O molecules to obtain abundant OH_{ads} species at a low overpotential, which can effectively remove CO_{ads} adsorbed on the Pt surface through electro-oxidation, thereby alleviating the CO-poisoning effect during alcohol electro-oxidation. This phenomenon is usually explained as the Watanabe−Motoo bifunctional mechanism.[17,18] Furthermore, recent works have revealed that the introduction of oxophilic metals (such as Ru and Sn) into Pt nanostructures can significantly enhance the capability to induce C−C bond cleavage with significant C_1 pathway selectivity for the EOR,[1,15] and thereby conducive to the complete oxidation of ethanol to CO_2. Therefore, we suggest that Pt-based nanocatalysts with rationally designed alloy phases could be further explored as promising electrocatalysts for C_{2+} alcohol electro-oxidation.

To date, Pt-based alloy catalysts including Pt−Sn,[15] Pt−Rh,[1] Pt−Fe,[19] Pt−Bi,[16] and Pt−Ni[20] have been reported for improved EOR catalytic activity and stability. Nevertheless, it is noteworthy that the non-platinum metal loss of a Pt−M alloy during the EOR in acidic operating environments leads to decreased durability, which is still an urgent challenge.[21] Among the non-platinum metals, Au has not only perfect stability in an acidic medium but also particular effects on Pt owing to its higher electronegativity than Pt.[14,22,23] Consequently, we propose that Pt−Au alloy catalysts with unique electronic and catalytic properties are promising for the application in direct alcohol fuel cells. Unfortunately, at present, most synthesis methods for Pt−Au nanostructures involve harsh conditions, complicated operations, and the addition of toxic surfactants.[14,22,24−26] Moreover, in most cases, these Pt−Au alloy catalysts have a core−shell structure with a low degree of alloying, and their diameters are usually tens of nanometers.[26−28] Generally, the particle size of the catalyst has better to be controlled at 6−10 nm, which can maximize the surface utilization of the Pt-based catalyst and also prevent the catalyst from being easily agglomerated and from undergoing Ostwald ripening.[29−31] On the other hand, the support materials can significantly affect the electrocatalytic performance. In comparison with common carbon black supports, nanocarbon materials, particularly carbon nanotubes (CNTs), have been regarded as promising support materials for catalysts due to their excellent conductivity and uniform dispersibility for catalyst nanoparticles (NPs).[23] The unique one-dimensional nanostructure and conductive network of CNTs can facilitate the dispersion and stabilization of the loaded catalyst through strong d−π interactions between the CNTs and catalyst NPs.[23,32−34] Therefore, it is imperative to develop a simple and mild method for the controllable preparation of a CNT-supported Pt−Au electrocatalyst with a high Pt alloying degree and an optimal electronic structure to boost the C_{2+} alcohol electro-oxidation.

Herein, we report the synthesis of Pt−Au NPs with tailored alloying degrees and adjustable particle diameters (4.6−7.9 nm) in situ grown on CNTs by a facile room-temperature reduction method as high-performance catalysts for C_{2+} alcohol electro-oxidation. The alloying degree and particle size of Pt−Au NPs were adjusted by adding different amounts of a metal precursor solution. Detailed experimental studies indicate that the introduction of Au into Pt nanostructures can essentially improve the electrocatalytic capability of C−C bond cleavage, which is beneficial to the increase in catalytic activity in acidic and basic media. The constructed $Pt_{45}Au_{55}$/CNTs catalyst with an optimal Pt alloying degree and diameter (6.3 nm) can essentially alleviate the CO poisoning of the catalyst and enhance the interaction between the catalytic active species and the support surface. Taking into account the aforementioned advantages, the Pt−Au catalyst exhibits excellent catalytic performance for the C_{2+} alcohol electro-oxidation.

EXPERIMENTAL SECTION

Chemicals and Materials. Hexachloroplatinic acid ($H_2PtCl_6·6H_2O$, 99.95%), chloroauric acid ($HAuCl_4·4H_2O$), and sodium borohydride ($NaBH_4$, ≥97.0%) were received from the First Regent Co. Ltd. (Shanghai, China). Ethanol (≥99.5%), H_2SO_4 (≥95.0%), sodium citrate ($C_6H_5Na_3O_7·2H_2O$, AR), and potassium hydroxide (KOH, AR) were all supplied by Chuandong Chemical Reagent Company (Chengdu, China). Nafion solution (5 wt %) was derived from DuPont China Holding Co., Ltd. Multiwalled CNTs were obtained from Cabot Co., Ltd. The commercial Pt/C catalyst (Pt/C-JM, 20 wt % Pt) was obtained from Johnson Matthey Company. Dimethylsulfoxide (DMSO, 99.95%) was purchased from Alfa Aesar. Deuteroxide (D_2O, 99.9%) was obtained from Sigma-Aldrich.

Synthesis of $Pt_{56}Au_{44}$/CNTs, $Pt_{50}Au_{50}$/CNTs, $Pt_{45}Au_{55}$/CNTs, $Pt_{42}Au_{58}$/CNTs, and $Pt_{38}Au_{62}$/CNTs Electrocatalysts. Pt−Au alloy NPs with different Pt/Au mass ratios supported on multiwalled carbon nanotubes were synthesized by a simple co-reduction process of sodium borohydride and sodium citrate at room temperature. For the synthesis of $Pt_{45}Au_{55}$/CNTs, 20 mg of CNTs was dispersed into 20 mL of deionized water through ultrasonication for approximately 1 h to form a uniform CNT suspension. Then, 10 mg of $NaBH_4$ was dissolved into 4 mL of H_2O with ultrasonication for approximately 10 min to form a $NaBH_4$ solution. Subsequently, 30 mg of $C_6H_5Na_3O_7·2H_2O$ was added into 5 mL of H_2O, followed by adding 0.298 mL of deionized water solution of 38.62 mM $H_2PtCl_6·6H_2O$ and 0.236 mL of ethylene glycol solution of 58.82 mM $HAuCl_4·4H_2O$ under ultrasonication for approximately 10 min to form a homogeneous mixture. Finally, the mixture was transferred dropwise into the above CNT suspension. After stirring for 30 min, the $NaBH_4$ solution was added dropwise to the suspension, followed by magnetic stirring for 24 h at room temperature. The resultant products were collected via filtration and washed with ethanol and H_2O. The synthesis processes for other Pt−Au/CNTs samples with different Pt/Au mass ratios ($Pt_{56}Au_{44}$/CNTs, $Pt_{50}Au_{50}$/CNTs, $Pt_{42}Au_{58}$/CNTs, and $Pt_{38}Au_{62}$/CNTs) were the same as that of $Pt_{45}Au_{55}$/CNTs by adjusting the amounts of added metal precursor solutions, and the total metal loading was 20 wt %. As two control samples, Au/CNTs and Pt/CNTs were prepared by the same method without the addition of $H_2PtCl_6·6H_2O$−water solution and $HAuCl_4·4H_2O$−ethylene glycol solution, respectively, and the theoretical loading content of the metal was 20 wt %.

Material Characterization. The accurate Pt and Au loadings of all samples (Table S1) were determined by inductively coupled plasma-optical emission spectroscopy (ICP-OES) (Optima 5300DV) by dissolving the as-prepared catalysts in a mixture of concentrated hydrochloric and nitric acids (V_{HCl}/V_{HNO_3} = 3:1). X-ray diffraction (XRD) analysis was performed on a powder X-ray diffractometer (Bruker D8 Advance) with a Cu Kα radiation source (λ = 1.5406 Å) at a scanning rate of 8° min^{-1}. Scanning electron microscopy (SEM) (FEI Nova NanoSEM 450) and transmission electron microscopy (TEM) (JEM-2100) were utilized for the surface morphology and structural characterization. Scanning TEM and elemental mapping images were detected using an SEM (Hitachi SU9000) equipped with an Oxford Ultim Extreme apparatus. The surface element compositions and valence states of all samples were analyzed using an X-ray photoelectron spectrometer (XPS) (PHI-5000 Versa Probe) equipped with a monochromatic Al Ka radiation source.

Electrochemical Analysis. All electrochemical measurements of catalysts were conducted on a standard three-electrode system with a CHI-760E electrochemical station. A Pt disk (1 × 1 cm^2) and a saturated calomel electrode (SCE, Hg/Hg_2Cl_2) were used as the counter and reference electrodes, respectively. A glassy carbon (GC)

https://doi.org/10.1021/acs.chemmater.1c00886
Chem. Mater. 2021, 33, 3767−3778

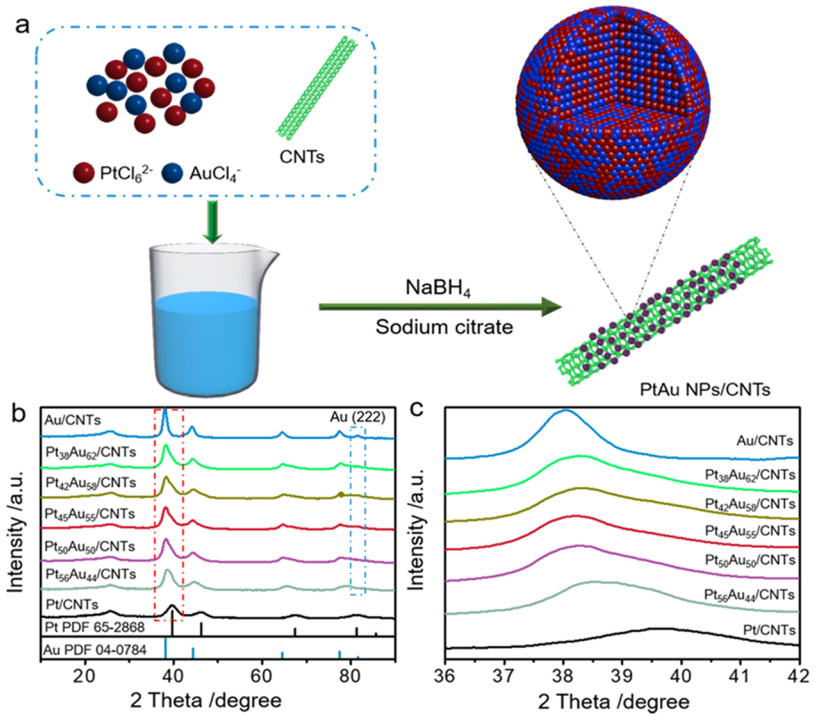

Figure 1. (a) Schematic illustration for the formation process of Pt−Au alloy NPs supported on CNTs. (b) XRD patterns of the Au/CNTs, $Pt_{38}Au_{62}$/CNTs, $Pt_{42}Au_{58}$/CNTs, $Pt_{45}Au_{55}$/CNTs, $Pt_{50}Au_{50}$/CNTs, $Pt_{56}Au_{44}$/CNTs, and Pt/CNTs catalysts. (c) Magnified XRD profiles of all samples in the 2θ angle range between 36 and 42°.

electrode with a diameter of 4 mm was utilized as the working electrode. For working electrode preparation, 2 mg of catalyst was dispersed into a mixture containing 500 μL of C_2H_5OH, 500 μL of H_2O, and 50 μL of a 5 wt % Nafion solution and sonicated for approximately 30 min to form a homogeneous catalyst ink. After that, 5 μL of the catalyst ink was loaded onto the GC surface and dried naturally. All electrolyte solutions were saturated with N_2 (≥99.999%) before any electrochemical measurement. All electrochemical potentials were reported with respect to the SCE.

Quantitative Analysis of Liquid Products. For liquid product quantification, the catalyst was pipetted onto a carbon paper electrode (1 × 1 cm^2) with an areal loading of 1.0 mg·cm^{-2}. After the chronoamperometric measurement at 0.7 V in a 0.5 M H_2SO_4 + 1.0 M C_2H_5OH solution for 7200 s, the electrolyte was collected for quantitative analysis by ^{1}H NMR (Bruker AV-600). Briefly, 600 μL of the electrolyte was uniformly mixed with 100 μL of D_2O and 100 μL of 10 μg·mL^{-1} DMSO as an internal standard. The one-dimensional ^{1}H spectrum was obtained with necessary suppression of water peaks by a water presaturation method. The concentration of CH_3COOH was determined by the standard curve using various concentrations (2, 4, 8, and 12 μg·mL^{-1}) of acetate and the internal standard (10 μg·mL^{-1} DMSO). The linear relationship between the known acetate concentration and the relative area (vs 10 μg·mL^{-1} DMSO) was made into a standard curve, as shown in Figure S1. The Faradaic efficiency (FE) of products can be calculated by the following equation: FE = $m \times n \times F/Q$, where m is the required electron number for generating one product molecule, n is the total amount of the liquid products (in moles), F is the Faraday constant, and Q is the total charge.

RESULTS AND DISCUSSION

As illustrated in Figure 1a, Pt−Au alloy NPs with different Pt/Au mass ratios decorated on CNTs were synthesized by a convenient co-reduction process of sodium borohydride and sodium citrate at room temperature. Figure 1b shows typical X-ray diffraction (XRD) patterns of the Pt/CNTs, $Pt_{56}Au_{44}$/CNTs, $Pt_{50}Au_{50}$/CNTs, $Pt_{45}Au_{55}$/CNTs, $Pt_{42}Au_{58}$/CNTs, $Pt_{38}Au_{62}$/CNTs, and Au/CNTs catalysts. The broad XRD peaks of all samples at approximately 25° are indexed to the (002) crystalline plane of the CNT support.[35] As shown in Figure 1c, the diffraction peaks of $Pt_{56}Au_{44}$/CNTs, $Pt_{50}Au_{50}$/CNTs, $Pt_{45}Au_{55}$/CNTs, $Pt_{42}Au_{58}$/CNTs, and $Pt_{38}Au_{62}$/CNTs located at approximately 39.8° are indexed to the (111) plane of alloy NPs, which are situated between those of Pt/CNTs and Au/CNTs, indicating that Au is incorporated into the Pt nanostructure to form an alloy phase.[24,36] Moreover, with the increase in the amount of added $HAuCl_4 \cdot 4H_2O$, the (111) plane diffraction peak positions gradually shift from the monometallic Pt phase toward the Au phase, illustrating that the Au fractions in the Pt−Au alloy nanostructure increase. This analysis result is consistent with the ICP-OES test results (Table S1). More importantly, as shown in Figure 1b, the peaks associated with the (222) plane of Au for $Pt_{56}Au_{44}$/CNTs and $Pt_{50}Au_{50}$/CNTs at 81.72° are not observed, demonstrating that Au exists as a Pt−Au alloy without a separate Au phase. However, as the amount of added $HAuCl_4 \cdot 4H_2O$ increases, the peak corresponding to the (222) plane of Au for the $Pt_{45}Au_{55}$/CNTs, $Pt_{42}Au_{58}$/CNTs, and $Pt_{38}Au_{62}$/CNTs hybrids is observed, indicating the presence of some excess Au phase and confirming that Pt exists entirely in the form of a Pt−Au alloy phase. This phenomenon illustrates that the alloying degree of Pt−Au NPs can be controllably adjusted by adding different amounts of the metal precursor solution.

The surface morphology of as-prepared samples was first characterized by field-emission scanning electron microscopy (SEM) (Figures S2 and S3). It is observed that the CNTs with a tubular structure and a diameter of approximately 20 nm are intertwined with each other to form a loose network structure. This structure is beneficial for accelerating the mass transfer process during alcohol electro-oxidation processes compared with the conventional carbon black as a catalyst support. Figures S2 and S3 show that the metal nanoparticles are

https://doi.org/10.1021/acs.chemmater.1c00886
Chem. Mater. 2021, 33, 3767−3778

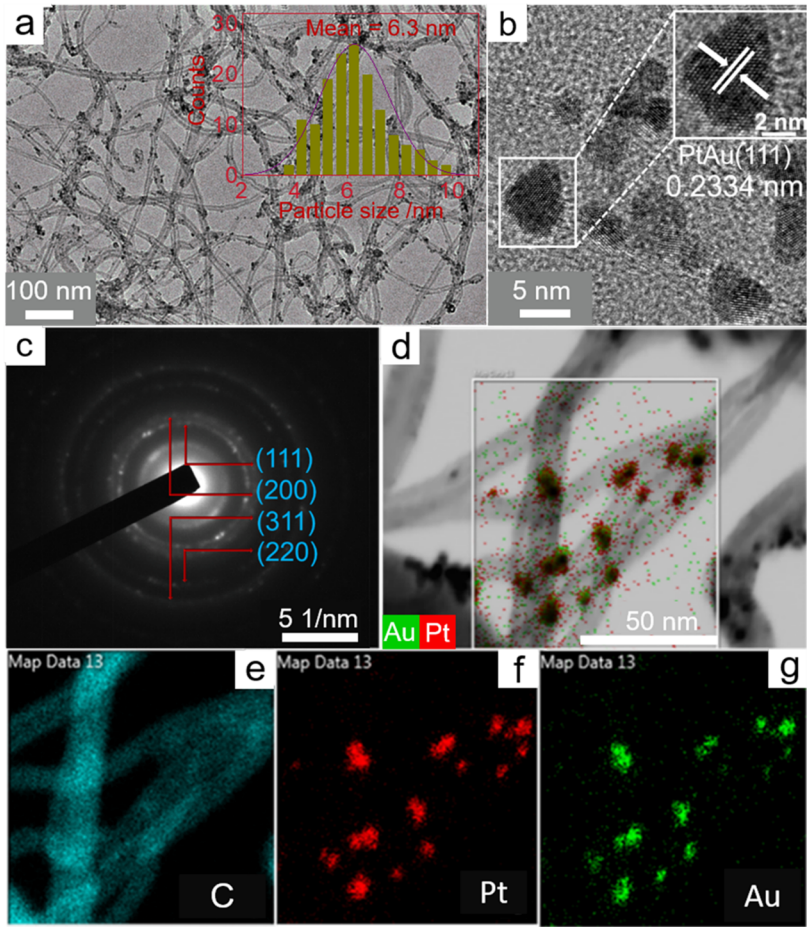

Figure 2. (a) TEM image of the $Pt_{45}Au_{55}$/CNTs catalyst. The inset in (a) shows the corresponding particle size distribution histograms. (b) HRTEM image, (c) SAED pattern, (d) scanning TEM, and (e–g) EDS elemental mapping images of the $Pt_{45}Au_{55}$/CNTs catalyst.

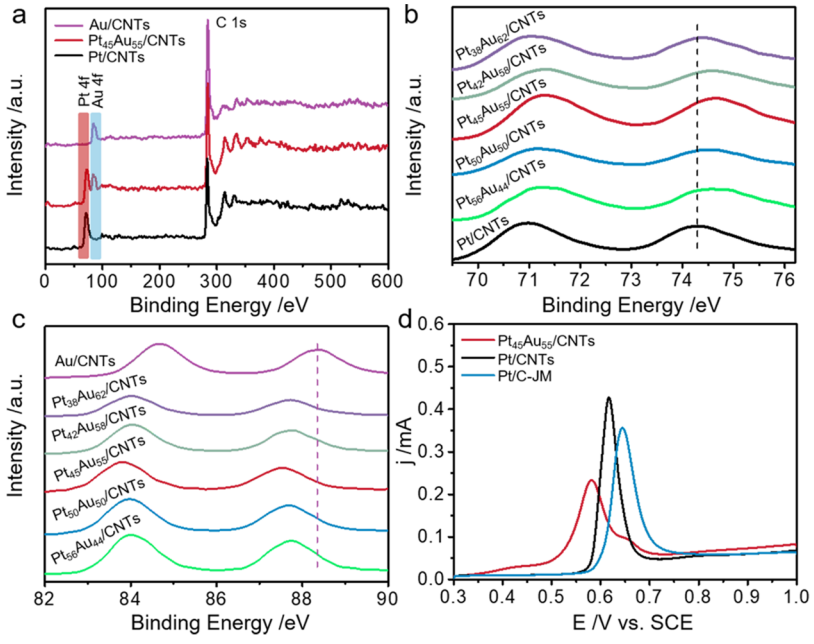

Figure 3. (a) Survey XPS profiles of the Au/CNTs, $Pt_{45}Au_{55}$/CNTs, and Pt/CNTs samples. (b) Pt 4f XPS spectra of the $Pt_{38}Au_{62}$/CNTs, $Pt_{42}Au_{58}$/CNTs, $Pt_{45}Au_{55}$/CNTs, $Pt_{50}Au_{50}$/CNTs, $Pt_{56}Au_{44}$/CNTs, and Pt/CNTs samples. (c) Au 4f XPS spectra of the Au/CNTs, $Pt_{38}Au_{62}$/CNTs, $Pt_{42}Au_{58}$/CNTs, $Pt_{45}Au_{55}$/CNTs, $Pt_{50}Au_{50}$/CNTs, and $Pt_{56}Au_{44}$/CNTs samples. (d) CO stripping voltammograms of the $Pt_{45}Au_{55}$/CNTs, Pt/CNTs, and Pt/C-JM catalysts in a 0.5 M H_2SO_4 solution at a scan rate of 50 $mV{\cdot}s^{-1}$.

https://doi.org/10.1021/acs.chemmater.1c00886
Chem. Mater. 2021, 33, 3767–3778

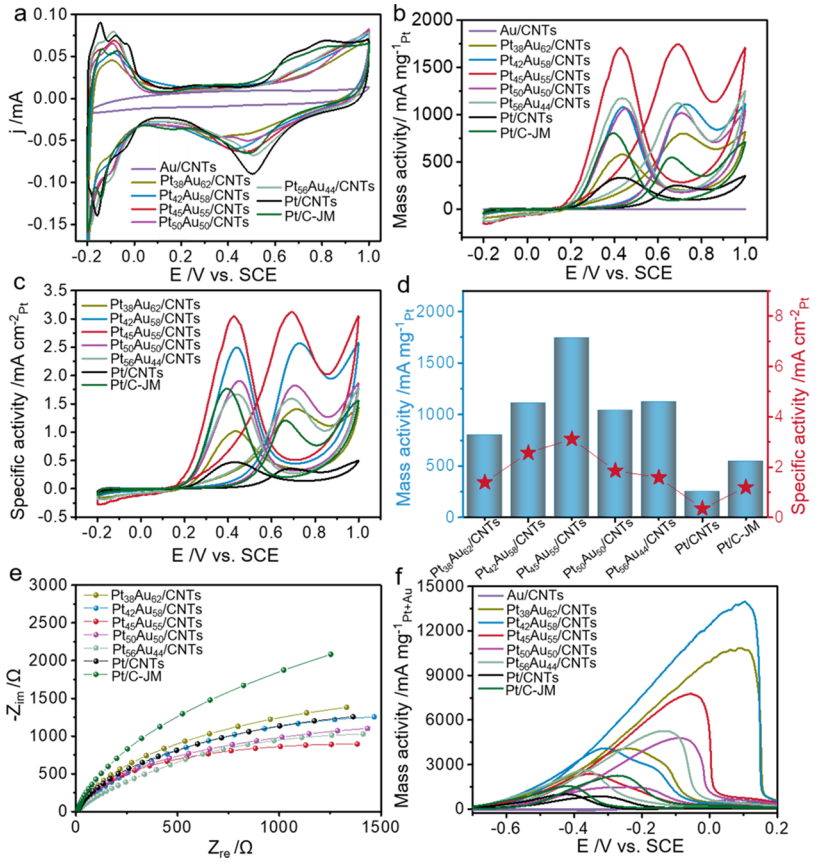

Figure 4. (a) CV curves of the Au/CNTs, $Pt_{38}Au_{62}$/CNTs, $Pt_{42}Au_{58}$/CNTs, $Pt_{45}Au_{55}$/CNTs, $Pt_{50}Au_{50}$/CNTs, $Pt_{56}Au_{44}$/CNTs, Pt/CNTs, and Pt/C-JM samples in a 0.5 M H_2SO_4 solution at a scan rate of 50 mV·s^{-1}. (b) Mass activity and (c) specific activity of these samples toward the EOR in a 0.5 M H_2SO_4 + 1.0 M C_2H_5OH solution. (d) Comparisons of the mass activity and specific activity of these samples in a 0.5 M H_2SO_4 + 1.0 M C_2H_5OH solution. (e) Nyquist plots of these samples in a 0.5 M H_2SO_4 + 1.0 M C_2H_5OH solution at 0.7 V. (f) CV curves of these catalysts in a 1.0 M KOH + 1.0 M C_2H_5OH solution at a scan rate of 50 mV·s^{-1}.

uniformly deposited on the surface of CNTs without obvious agglomeration. Moreover, the compositions were further analyzed by the elemental mapping of energy-dispersive X-ray spectroscopy (EDS), as shown in Figure S2c–f. It can be clearly seen that the Pt and Au components of $Pt_{45}Au_{55}$/CNTs are evenly distributed over the carbon support surface.

The microstructure of Pt–Au alloy NPs was then characterized by field-emission transmission electron microscopy (TEM). As shown in Figure 2a, $Pt_{45}Au_{55}$ NPs were uniformly distributed over the whole surface of CNTs, and the average particle distribution (the inset in Figure 2a) was centered at approximately 6.3 nm. In addition, the TEM images of the Pt/CNTs, $Pt_{56}Au_{44}$/CNTs, $Pt_{50}Au_{50}$/CNTs, $Pt_{42}Au_{58}$/CNTs, $Pt_{38}Au_{62}$/CNTs, and Au/CNTs catalysts are presented in Figure S4. It can be clearly observed that the particle size of Pt–Au alloy NPs gradually increases as the amount of added Au increases. The average particle sizes of Pt–Au alloy NPs are in the range of 4.6–7.9 nm (Figure S4), which are between the diameters of pristine Pt NPs (4.1 nm) and Au NPs (12 nm). This result further confirms that the particle size of Pt–Au alloy catalysts can be easily regulated by adjusting the amount of the added $HAuCl_4{\cdot}4H_2O$ precursor (Figure 7a). The high-resolution TEM (HRTEM) images (the inset in Figures 2b and S5a) of $Pt_{45}Au_{55}$/CNTs show a lattice spacing of 0.2334 nm that can be indexed to the Pt–Au(111) plane, which is slightly larger than the lattice spacing of the Pt/CNTs catalyst (0.2230 nm, Figure S5b). This result further confirms that the Au phase is incorporated into the Pt nanostructures for the $Pt_{45}Au_{55}$/CNT catalyst, which is in agreement with the XRD analysis results. On the other hand, the selective area electron diffraction (SAED) pattern of $Pt_{45}Au_{55}$/CNTs (Figure 2c) exhibits several bright rings, which are assigned to the (111), (200), (220), and (311) planes of the Pt–Au alloy nanostructures, respectively. Furthermore, the elemental distribution was also probed by scanning TEM and EDS mapping (Figure 2d–g), confirming that Pt and Au species were uniformly distributed over the Pt–Au alloy NPs loaded on the CNTs. These results demonstrated that a Pt–Au alloy nanostructure was synthesized rather than a simple core–shell structure or a mixture of Pt and Au NPs via the mild and convenient room-temperature reduction method.

The elemental compositions and valence states of all samples were analyzed by X-ray photoelectron spectroscopy (XPS). The binding energies (BE) of all peaks were calibrated to the C 1s peak at 284.6 eV.[35] The survey spectra of the samples are shown in Figures 3a and S6, and the signal peaks of C 1s, Pt 4f, and Au 4f bands can be clearly observed. Figure S6 shows that as the amount of added Au precursor increases, the intensity of Pt 4f XPS spectra gradually decreases, while the intensity of Au 4f XPS spectra for Pt–Au alloy samples gradually increases. This phenomenon indicates that as the amount of added Au precursor increases, the atomic content of Pt in the Pt–Au alloy NPs gradually decreases, while the atomic content of Au increases. Figure S7 shows the

https://doi.org/10.1021/acs.chemmater.1c00886
Chem. Mater. 2021, 33, 3767–3778

normalized high-resolution Pt 4f XPS spectra of the Pt/CNTs, $Pt_{56}Au_{44}$/CNTs, $Pt_{50}Au_{50}$/CNTs, $Pt_{45}Au_{55}$/CNTs, $Pt_{42}Au_{58}$/CNTs, and $Pt_{38}Au_{62}$/CNTs samples, and the characteristic peaks could be fitted into two pairs of doublets associated with Pt^0 and Pt^{2+}.[37−39] The relative ratios of Pt^0 and Pt^{2+} species are calculated by the integral areas of deconvoluted XPS peaks, as compared in Table S2. Similarly, the normalized high-resolution Au 4f XPS spectra (Figure S8) of the Au/CNTs, $Pt_{56}Au_{44}$/CNTs, $Pt_{50}Au_{50}$/CNTs, $Pt_{45}Au_{55}$/CNTs, $Pt_{42}Au_{58}$/CNTs, and $Pt_{38}Au_{62}$/CNTs samples are decomposed into two pairs of doublets, which are assigned to Au^0 and Au^{3+}, respectively,[40] and the relative ratios of Au^0 and Au^{3+} species are presented in Table S3. Furthermore, the Pt 4f BE of the $Pt_{56}Au_{44}$/CNTs, $Pt_{50}Au_{50}$/CNTs, $Pt_{45}Au_{55}$/CNTs, $Pt_{42}Au_{58}$/CNTs, and $Pt_{38}Au_{62}$/CNTs samples show blue shifts in comparison with that of the Pt/CNTs sample (Figure 3b). In contrast, the Au 4f BE of the $Pt_{56}Au_{44}$/CNTs, $Pt_{50}Au_{50}$/CNTs, $Pt_{45}Au_{55}$/CNTs, $Pt_{42}Au_{58}$/CNTs, and $Pt_{38}Au_{62}$/CNTs samples show red shifts compared with that of the Au/CNTs sample (Figure 3c). These results confirm the electron transfer from Pt to Au.[22] The strong electron interactions between Pt and Au can effectively modify the electronic state and the physical−chemical properties of the Pt−Au alloy NPs. Additionally, previous studies[10,11] have reported that the blue shift of Pt 4f BE can lead to a decrease in the affinity between CO_{ads} and the Pt surface, owing to the weakening of the feedback π bonds between the active metals and toxic intermediates. As a result, the Pt−Au alloy catalysts possess excellent CO resistance. To identify the anti-CO poisoning ability of the Pt−Au alloy catalysts, CO-stripping experiments were carried out in a N_2-saturated 0.5 M H_2SO_4 solution. As shown in Figures 3d and S9a, the onset potentials and peak potentials of the $Pt_{56}Au_{44}$/CNTs (0.547 and 0.596 V), $Pt_{50}Au_{50}$/CNTs (0.510 and 0.582 V), $Pt_{45}Au_{55}$/CNTs (0.528 and 0.591 V), $Pt_{42}Au_{58}$/CNTs (0.549 and 0.607 V), and $Pt_{38}Au_{62}$/CNTs (0.541 and 0.586 V) catalysts for CO oxidation are more negative than those of Pt/CNTs (0.563 and 0.617 V) and commercial Pt/C catalysts (Pt/C-JM, with 20 wt % Pt, Johnson Matthey Corp.) (0.570 and 0.645 V), respectively. These analysis results demonstrate that Au incorporated into Pt nanostructures can greatly improve the ability of the catalyst to resist CO poisoning, thus beneficial for refreshing the active sites on the alloy surface during the alcohol electro-oxidation processes.[17,21]

The electrochemical behavior of all samples was investigated via cyclic voltammetry (CV) tests in a 0.5 M H_2SO_4 solution. As shown in Figure 4a, all CV curves show the characteristic peaks of hydrogen adsorption and desorption between −0.2 and 0.1 V. Specifically, two hydrogen desorption peaks at approximately −0.15 and −0.08 V are associated with the catalytic effects of the Pt(111) and (100) planes, respectively.[38] It is clearly observed that the intensity of the hydrogen desorption peaks of $Pt_{56}Au_{44}$/CNTs, $Pt_{50}Au_{50}$/CNTs, $Pt_{45}Au_{55}$/CNTs, $Pt_{42}Au_{58}$/CNTs, and $Pt_{38}Au_{62}$/CNTs at approximately −0.15 V gradually decreases relative to that of Pt/CNTs and Pt/C-JM (Figure 4a). This phenomenon is ascribed to the decrease of the Pt atomic content that reduces the amount of hydrogen adsorption sites. Moreover, the electrochemical surface area (ECSA) of all samples is evaluated according to the following equation:[37] $ECSA = S/(m \times q_H \times V)$, where S is the integral area of the hydrogen desorption region after deducting the double layer, m is the mass of Pt on the glassy carbon electrode, V is the scan speed, and q_H (210 $\mu C \cdot cm^{-2}$) is the charge required for desorbing the monolayer of adsorbed hydrogen per square centimeter of the Pt surface. As summarized in Table S4, the calculated ECSA values of the Pt−Au alloy catalysts are lower than that of Pt/CNTs because Au has no contribution to hydrogen absorption and desorption (Figure 4a).

The catalytic activities of all catalysts for the EOR were investigated in a 0.5 M H_2SO_4 + 1.0 M C_2H_5OH electrolyte, as shown in Figure 4b,c. It is clearly observed that Au/CNTs shows no catalytic activity for the EOR in acidic medium; however, the introduction of Au into the Pt nanostructure significantly promotes the catalytic activity of the Pt−Au alloy (Figure 4b). It is generally accepted that the I_f/I_b ratios (where I_f is the forward current density and I_b is the backward current density) reflect the anti-CO poisoning ability of the catalysts.[1] The higher I_f/I_b value indicates higher CO tolerance. As shown in Figure S9b, the I_f/I_b ratios of $Pt_{56}Au_{44}$/CNTs (0.95), $Pt_{50}Au_{50}$/CNTs (0.98), $Pt_{45}Au_{55}$/CNTs (1.02), $Pt_{42}Au_{58}$/CNTs (1.03), and $Pt_{38}Au_{62}$/CNTs (1.38) are higher than those of Pt/C-H (0.75) and Pt/C-JM (0.68), confirming that the introduction of Au into Pt nanostructures can effectively improve the CO tolerance; this result is in line with that of the CO-stripping experiments. Figure 4d shows that the mass ratio of Pt/Au affects the catalytic activity of the Pt−Au alloy catalyst for EOR, and an optimal ratio of Pt/Au was found to be 45:55 ($Pt_{45}Au_{55}$/CNTs). The excellent catalytic performance of the $Pt_{45}Au_{55}$/CNTs catalyst compared with other Pt−Au alloy catalysts may be due to the optimal Pt alloy degree and the strong electronic interaction between Pt and Au. Specifically, XRD analysis results shows that as the atomic content of Au increases to a certain amount such as $Pt_{45}Au_{55}$/CNTs, $Pt_{42}Au_{58}$/CNTs, and $Pt_{38}Au_{62}$/CNTs, excess Au phases will separate out (Figure 1b). Although the Au incorporated into the Pt nanostructure is beneficial for enhancing the catalytic performance, excessive separate Au phases such as $Pt_{42}Au_{58}$/CNTs and $Pt_{38}Au_{62}$/CNTs will cover the active sites of Pt owing to the Au phase showing no catalytic activity for the EOR in acidic medium. Moreover, Figure 3b shows that the Pt 4f binding energy blue shifts for $Pt_{45}Au_{55}$/CNTs are more than those of the other Pt−Au alloy samples, which indicates that there is strong electronic interaction between Pt and Au atoms on the $Pt_{45}Au_{55}$/CNTs catalyst. The strong electronic interaction between Pt and Au weakens the feedback π bond between Pt and CO, which is beneficial for regaining the Pt active sites during the EOR and increasing the catalytic efficiency.[9,11] Therefore, $Pt_{45}Au_{55}$/CNTs exhibits the highest catalytic activity for the EOR compared with other Pt−Au alloy samples (Figure 4b,c). Additionally, the mass activity of $Pt_{45}Au_{55}$/CNTs (1746 $mA \cdot mg_{Pt}^{-1}$) is approximately 7- and 3.2-fold better than those of Pt/C-H (251 $mA \cdot mg_{Pt}^{-1}$) and Pt/C-JM (546 $mA \cdot mg_{Pt}^{-1}$), respectively. The specific activity of all samples was also calculated as the current density normalized to the ECSA of each catalyst (Figure 4c). The specific activity of $Pt_{45}Au_{55}$/CNTs is 3.12 $mA \cdot cm_{Pt}^{-2}$, which is almost 8.9- and 2.6-fold higher than those of Pt/C-H (0.35 $mA \cdot cm_{Pt}^{-2}$) and Pt/C-JM (1.20 $mA \cdot cm_{Pt}^{-2}$), respectively. Table S5 shows that the mass activity of $Pt_{45}Au_{55}$/CNTs for the EOR in acidic media is very competitive among other recently reported Pt-based catalysts. To obtain more insights into the reasons for the excellent catalytic activity of the $Pt_{45}Au_{55}$/CNTs catalyst in acidic medium, electrochemical impedance spectroscopy (EIS) measurements of all catalysts were carried out (Figure 4e). It is universally recognized that the diameter of the semicircle in the

https://doi.org/10.1021/acs.chemmater.1c00886
Chem. Mater. 2021, 33, 3767−3778

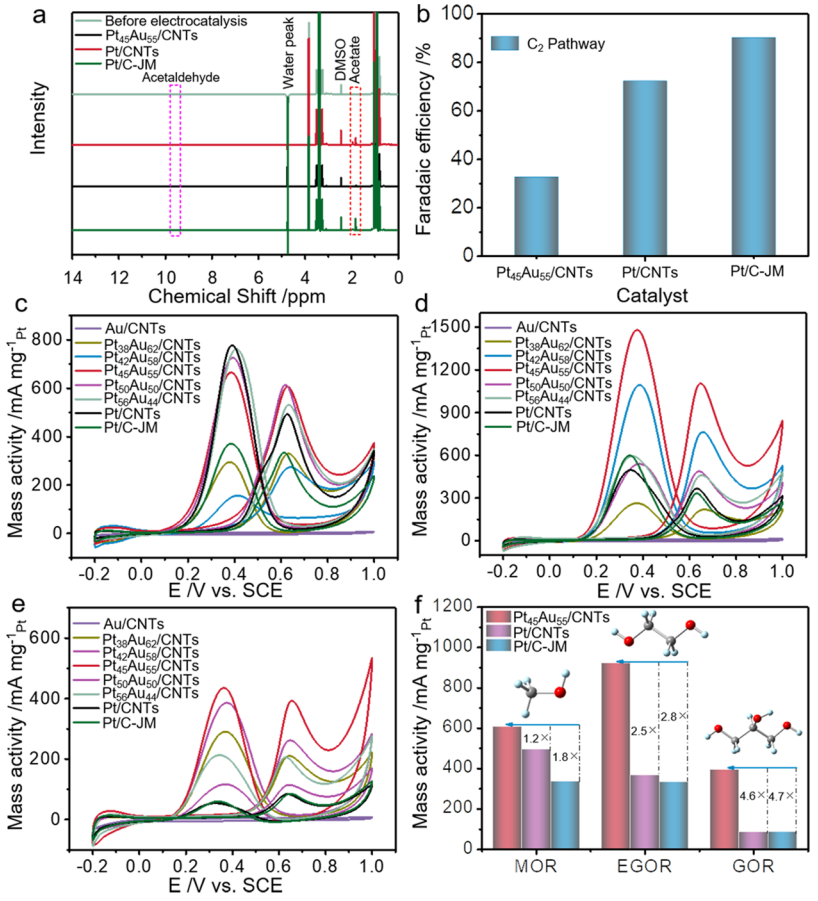

Figure 5. (a) ^{1}H NMR spectra of the electrolyte before electrocatalysis and after 7200 s of a chronoamperometric measurement at 0.7 V for the $Pt_{45}Au_{55}$/CNTs, Pt/CNTs, and Pt/C-JM samples. (b) Faradaic efficiencies of the C_2 pathways for the $Pt_{45}Au_{55}$/CNTs, Pt/CNTs, and Pt/C-JM samples. (c–e) CV curves of the Au/CNTs, $Pt_{38}Au_{62}$/CNTs, $Pt_{42}Au_{58}$/CNTs, $Pt_{45}Au_{55}$/CNTs, $Pt_{50}Au_{50}$/CNTs, $Pt_{56}Au_{44}$/CNTs, Pt/CNTs, and Pt/C-JM samples in (c) 0.5 M H_2SO_4 + 1.0 M CH_3OH, (d) 0.5 M H_2SO_4 + 1.0 M CH_2OHCH_2OH, and (e) 0.5 M H_2SO_4 + 1.0 M $CH_2OHCH_2OHCH_2OH$. (f) Comparisons of the mass activity of the $Pt_{45}Au_{55}$/CNTs, Pt/CNTs, and Pt/C-JM catalysts toward the methanol oxidation reaction (MOR), ethylene glycol oxidation reaction (EGOR), and glycerol oxidation reaction (GOR).

Nyquist curve is proportional to the charge-transfer resistance (R_{ct}), which has an approximately inverse relationship with the catalytic activity.[37] The smaller the diameter of the semicircle, the lower the R_{ct} and the higher the catalytic activity. The diameter of the semicircle for the $Pt_{45}Au_{55}$/CNTs catalyst is smaller than those of other samples, demonstrating the excellent ethanol electro-oxidation activity of $Pt_{45}Au_{55}$/CNTs in acidic medium. This phenomenon is in accordance with the above EOR test results in 0.5 M H_2SO_4 + 1.0 M C_2H_5OH. Interestingly, the R_{ct} of Pt/CNTs is also lower than that of Pt/C-JM, which could be ascribed to the highly conductive CNT network that enables easy electrolyte infiltration and facilitates the mass transfer process during the EOR.

In addition, the catalytic activities of all samples for the EOR were also evaluated in an alkaline medium (1.0 M KOH + 1.0 M C_2H_5OH solution) (Figure 4f). Considering that the Au/CNTs sample also shows a weak catalytic activity (421 mA·mg_{Au}^{-1}) for the EOR in alkaline medium (Figure S10), the mass activity of each catalyst is calculated as the peak current density in the forward sweeps normalized to the sum of the loading weights of Pt and Au. Excellent mass activities are achieved by the Pt–Au alloy catalysts, including $Pt_{45}Au_{55}$/CNTs (7772 mA·mg_{Pt+Au}^{-1}), $Pt_{42}Au_{58}$/CNTs (13 993 mA·mg_{Pt+Au}^{-1}), and $Pt_{38}Au_{62}$/CNTs (10 855 mA·mg_{Pt+Au}^{-1}). The mass activity of $Pt_{42}Au_{58}$/CNTs (13 993 mA·mg_{Pt+Au}^{-1}) is approximately 33, 14, and 6 times as large as those of Au/CNTs (421 mA·mg_{Au}^{-1}), Pt/CNTs (1020 mA·mg_{Pt}^{-1}), and Pt/C-JM (2258 mA·mg_{Pt}^{-1}), respectively. Figure S11 shows that the as-measured mass activities of $Pt_{45}Au_{55}$/CNTs, $Pt_{42}Au_{58}$/CNTs, and $Pt_{38}Au_{62}$/CNTs are superior to other recently reported Pt-,[41,42] Pd-,[43−48] and Rh-[49]based catalysts in alkaline media.

To understand the reason for the superior catalytic performance of $Pt_{45}Au_{55}$/CNTs for EOR, the activation energies (E_a) of the $Pt_{45}Au_{55}$/CNTs, Pt/CNTs, and Pt/C-JM catalysts were calculated by Arrhenius plots measured in 0.5 M H_2SO_4 + 1.0 M C_2H_5OH.[1,15] As shown in Figure S12, the E_a value of $Pt_{45}Au_{55}$/CNTs at 0.7 V vs SCE is 50.10 kJ·mol^{-1}, which is higher than those of Pt/CNTs (37.29 kJ·mol^{-1}) and Pt/C (37.29 kJ·mol^{-1}). This phenomenon occurs because Au has no catalytic activity for the oxidative dehydrogenation of ethanol in acidic medium; hence, the formation of the Pt–Au alloy decreases the number of effective collisions between ethanol molecules and the Pt surface. Moreover, compared to the great performance improvement of the Pt–Au alloy NPs toward C_{2+} alcohol electro-oxidation, the electrocatalytic capability of Pt–Au alloy NPs for boosting the cleavage of B–H, N–H, C–H, and N–B bonds of other typical high-energy-density fuel molecules in alkaline medium, including $NaBH_4$, $NH_3{\cdot}H_2O$, $CH_3{\cdot}NH_2$, and $NH_3{\cdot}BH_3$, is not

https://doi.org/10.1021/acs.chemmater.1c00886
Chem. Mater. 2021, 33, 3767−3778

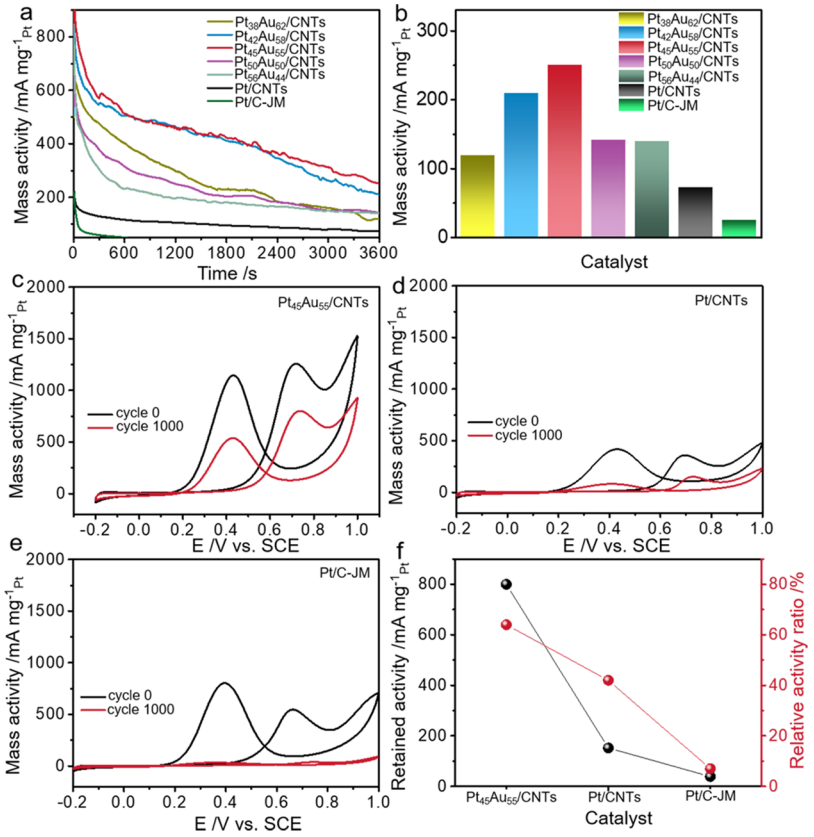

Figure 6. (a) Chronoamperometric curves of the samples in a 0.5 M H_2SO_4 + 1.0 M C_2H_5OH solution. (b) Retained mass activities of the samples after 3600 s of the chronoamperometric test at 0.6 V. (c–e) CV curves of the (c) $Pt_{45}Au_{55}$/CNTs, (d) Pt/CNTs, and (e) Pt/C-JM catalysts before and after 1000 cycles at a scan rate of 100 mV·s^{-1} in a 0.5 M H_2SO_4 + 1.0 M C_2H_5OH solution. (f) Comparison of the retained mass activities and relative activity ratios of $Pt_{45}Au_{55}$/CNTs, Pt/CNTs, and Pt/C-JM after the 1000-cycle ADT.

very significant (Figure S13). To further reveal the reasons for the excellent electrocatalytic performance of $Pt_{45}Au_{55}$/CNTs, the ethanol electro-oxidation products of the $Pt_{45}Au_{55}$/CNTs, Pt/CNTs, and Pt/C-JM catalysts were analyzed by nuclear magnetic resonance (NMR). The main C_2 products were found to be only acetate without acetaldehyde (Figure 5a). The faraday efficiency (FE) of CH_3COOH for the above three samples was calculated accordingly. Specifically, the FE (Figure 5b) of the C_2 pathway for $Pt_{45}Au_{55}$/CNTs is 32.74%, which is clearly less than those of Pt/CNTs (72.33%) and Pt/C-JM (90.32%), demonstrating that the incorporation of Au into Pt nanostructures can effectively improve the ability to catalyze the cleavage of C–C bonds during the EOR, thereby facilitating the complete oxidation of ethanol to carbon dioxide.

To confirm this hypothesis, the catalytic activities of all samples toward other C_1–C_3 alcohol molecules, including the methanol oxidation reaction (MOR, C_1 alcohol oxidation), ethylene glycol oxidation (EGOR, C_2 alcohol oxidation), and glycerol oxidation reaction (GOR, C_3 alcohol oxidation), were also investigated by CV tests (Figure 5c–e). Figure 5f shows that the mass activity of $Pt_{45}Au_{55}$/CNTs for MOR (607 mA·mg_{Pt}^{-1}) is 1.2- and 1.8-fold greater than those of Pt/CNTs (494 mA·mg_{Pt}^{-1}) and Pt/C-JM (335 mA·mg_{Pt}^{-1}), respectively. In the case of EGOR, the catalytic activity of $Pt_{45}Au_{55}$/CNTs (922 mA·mg_{Pt}^{-1}) is 2.5- and 2.8-fold higher than those of Pt/CNTs (366 mA·mg_{Pt}^{-1}) and Pt/C-JM (333 mA·mg_{Pt}^{-1}), respectively. More importantly, the mass activity of $Pt_{45}Au_{55}$/CNTs for GOR (393 mA·mg_{Pt}^{-1}) is 4.6- and 4.7-fold better than those of Pt/CNTs (85.73 mA·mg_{Pt}^{-1}) and Pt/C-JM (84.36 mA·mg_{Pt}^{-1}), respectively. As expected, for the methanol, ethanol, ethylene glycol, and glycerol electro-oxidation reactions, when the number of C–C bonds in the alcohol molecules increases, the alcohol oxidation activity of $Pt_{45}Au_{55}$/CNTs is multiplied compared with that of pure Pt-based catalysts, such as Pt/CNTs and Pt/C-JM. This evidence further confirms that the formation of the Pt–Au alloy phase is conducive to the oxidative fracture of the C–C bonds in C_{2+} alcohol molecules, which is beneficial to the complete oxidation of ethanol to CO_2. This phenomenon is analogous to the previous reports that the incorporation of non-Pt metals (such as Rh and Sn) in Pt nanostructures is beneficial for adsorbing β-C, and the neighboring Pt can adsorb the α-C of C_2H_5OH;[1,15] consequently, the Pt-based alloy phase can facilitate C–C bond cleavage for the EOR. It can be deduced that the introduction of Au into Pt nanostructures is also helpful for the adsorption of β-C; hence, the Pt–Au alloy catalysts significantly enhance the capability for C–C bond cleavage during C_{2+} alcohol electro-oxidation processes.

The durability of all catalysts for the EOR was evaluated by chronoamperometric measurements at 0.6 V for 3600 s in a 0.5 M H_2SO_4 + 1.0 M C_2H_5OH solution (Figure 6a). The retained mass activities of all samples after the chronoamperometric test are shown in Figure 6b. It is clearly seen that the $Pt_{56}Au_{44}$/CNTs (140 mA·mg_{Pt}^{-1}), $Pt_{50}Au_{50}$/CNTs (142 mA·mg_{Pt}^{-1}), $Pt_{45}Au_{55}$/CNTs (251 mA·mg_{Pt}^{-1}), $Pt_{42}Au_{58}$/CNTs (210 mA·mg_{Pt}^{-1}), and $Pt_{38}Au_{62}$/CNTs (120 mA·mg_{Pt}^{-1}) catalysts maintain higher mass activity in comparison with the Pt/

https://doi.org/10.1021/acs.chemmater.1c00886
Chem. Mater. 2021, 33, 3767–3778

CNTs (73.4 mA·mg_{Pt}^{-1}) and Pt/C-JM (25.4 mA·mg_{Pt}^{-1}) catalysts. This result suggests that the introduction of Au into Pt nanostructures is capable of reducing the poisoning effect and improving the catalytic durability during the EOR. Additionally, the stabilities of the $Pt_{45}Au_{55}$/CNTs, Pt/CNTs, and Pt/C-JM catalysts were investigated by a 1000-cycle accelerated durability test (ADT) (Figure 6c−e). Obviously, as shown in Figure 6f, the $Pt_{45}Au_{55}$/CNTs catalyst exhibits a higher retained catalytic activity (800 mA·mg_{Pt}^{-1}) and relative activity ratio (64%) than those of Pt/CNTs (152 mA·mg_{Pt}^{-1}, 42%) and Pt/C-JM (39 mA·mg_{Pt}^{-1}, 7%) catalysts, which further confirms the better durability of the $Pt_{45}Au_{55}$/CNTs catalyst.

To further reveal the reasons for the better stability of the $Pt_{45}Au_{55}$/CNTs catalyst during the EOR, the morphology and structure of $Pt_{45}Au_{55}$/CNTs and Pt/CNTs after the 1000-cycle ADT were investigated via TEM. As shown in Figure S14a,b, the density and particle size of $Pt_{45}Au_{55}$ NPs loaded on the CNTs after the stability test exhibit no obvious changes in comparison with those of the $Pt_{45}Au_{55}$/CNTs catalyst before the test (Figure 2a). However, for the Pt/CNTs catalyst (Figure S14c,d), serious aggregation of Pt NPs and the increase of particle size can be clearly observed after the 1000-cycle ADT by comparing with the TEM images (Figure S4a) of Pt/CNTs before the ADT. This suggests that one of the possible reasons for the performance degradation of Pt/CNTs is the aggregation of Pt NPs owing to the higher surface energy of Pt NPs than the Pt−Au alloy NPs. Notably, the stability of Pt/CNTs is still better than that of Pt/C-JM, probably because the dispersibility of Pt NPs on CNT support is better than that in carbon black, and the network structure of conductive CNTs accelerates the charge and mass transfer. This result is consistent with the previous studies that the electronic structure of graphitic carbon supports can largely facilitate strong d−π interactions between metal NPs and the support material.[23,32] This strong interaction leads to better dispersion and stabilization of metal NPs on the CNT surface.

The rationally designed Pt−Au/CNTs catalysts are expected to be promising highly efficient electrocatalysts for the C_{2+} alcohol electro-oxidation, as summarized by the following merits. First, the optimized electronic structure and particle size (Figure 7a) can not only maximize the surface utilization but also prevent the catalyst from undergoing Ostwald ripening and being easily agglomerated during the alcohol electro-oxidation processes. Meanwhile, the d−π interaction between the Pt−Au alloy NPs and CNTs leads to better dispersion and stabilization of alloy NPs. Second, as shown in Figure 7b, the strong electron interactions between Pt and Au can effectively modify the electronic state of the catalyst surface. Specifically, the electron transfer from Pt to Au greatly weakens the feedback π bonds between the CO_{ads} and active metals, and thus can decrease the affinity between CO_{ads} and the alloy surface, consequently possessing excellent CO resistance capability.[10,11] Third, the introduction of Au into the Pt nanostructure is conducive to enhancing the decomposition of H_2O to produce abundant −OH species, which can quickly oxidize/remove the toxic intermediates and then re-expose the active sites on the alloy surface during the C_{2+} alcohol electro-oxidation processes.[39,50,51] This phenomenon could be explained as a modified Watanabe−Motoo bifunctional mechanism with EOR as an example.

$$Au + H_2O \rightarrow Au - OH + H^+ + e^- \quad (1)$$

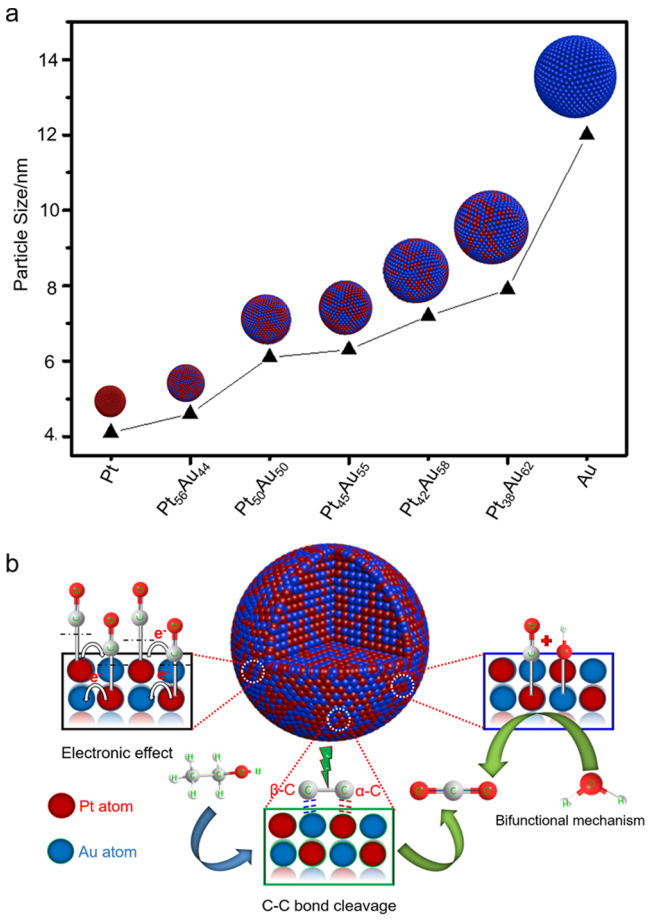

Figure 7. (a) Variations in alloying degree and particle size of the Pt, Pt−Au alloy, and Au NPs formed on CNTs by adjusting the amount of the added $HAuCl_4{\cdot}4H_2O$ precursor solution. (b) Schematic reaction mechanism of C_{2+} alcohol electro-oxidation processes on Pt−Au alloy catalysts.

$$2Pt + C_2H_5OH + H_2O \rightarrow 2\,Pt - (CO)_{ads} + 8\,H^+ + 8e^- \quad (2)$$

$$2Au - OH + Pt - (CO)_{ads} \rightarrow 2Au + Pt + H_2O + CO_2 \quad (3)$$

As a result, the Pt−Au alloy NPs loaded on CNTs exhibit significant performance improvement for complete electro-oxidation of alcohols to CO_2 by promoting the breakage of C−C bonds in C_{2+} alcohol molecules. Moreover, it is suggested that direct C_{2+} alcohol fuel cells can combine with low-cost and large-scale energy storage devices to provide green, sustainable, and reliable hybrid power supplies.[52,53]

■ CONCLUSIONS

In summary, we demonstrate the synthesis of a variety of Pt−Au alloy NPs with regulated alloying degrees and tailored electronic structures that were in situ grown on CNTs by a simple and mild room-temperature reduction method. The electronic state and particle size of the Pt−Au alloy NPs were optimized to alleviate the aggregation problem and the occurrence of Ostwald ripening. In-depth material characterization and electrochemical analyses revealed that the incorporation of Au into the Pt nanostructure could essentially improve the electrocatalytic capability for C−C bond cleavage

https://doi.org/10.1021/acs.chemmater.1c00886
Chem. Mater. 2021, 33, 3767−3778

during the C_{2+} alcohol electro-oxidation processes and enhance the tolerance against CO poisoning. Detailed comparisons of the oxidation activity in different C_1−C_3 alcohols and the quantitative analysis of final C_2 oxidation products confirm the excellent C−C bond cleavage capability of the Pt−Au alloy/CNTs catalysts, especially the $Pt_{45}Au_{55}$/CNTs sample. This work suggests that the rational design of the Pt alloy phase and support material is a promising route to develop advanced electrocatalysts toward high-efficiency direct alcohol fuel cells.

■ ASSOCIATED CONTENT

Supporting Information

The Supporting Information is available free of charge at https://pubs.acs.org/doi/10.1021/acs.chemmater.1c00886.

SEM, EDS, TEM, XPS, CV, and ICP-OES characterizations and performance comparisons of the samples (Figures S1−S14 and Tables S1−S5) (PDF)

■ AUTHOR INFORMATION

Corresponding Author

Zhong Jin − *MOE Key Laboratory of Mesoscopic Chemistry, MOE Key Laboratory of High Performance Polymer Materials and Technology, Jiangsu Key Laboratory of Advanced Organic Materials, School of Chemistry and Chemical Engineering, Nanjing University, Nanjing, Jiangsu 210023, China; Shenzhen Research Institute of Nanjing University, Shenzhen 518063, China;* orcid.org/0000-0001-8860-8579; Email: zhongjin@nju.edu.cn

Authors

Minghang Jiang − *MOE Key Laboratory of Mesoscopic Chemistry, MOE Key Laboratory of High Performance Polymer Materials and Technology, Jiangsu Key Laboratory of Advanced Organic Materials, School of Chemistry and Chemical Engineering, Nanjing University, Nanjing, Jiangsu 210023, China*

Yi Hu − *MOE Key Laboratory of Mesoscopic Chemistry, MOE Key Laboratory of High Performance Polymer Materials and Technology, Jiangsu Key Laboratory of Advanced Organic Materials, School of Chemistry and Chemical Engineering, Nanjing University, Nanjing, Jiangsu 210023, China*

Wenjun Zhang − *MOE Key Laboratory of Mesoscopic Chemistry, MOE Key Laboratory of High Performance Polymer Materials and Technology, Jiangsu Key Laboratory of Advanced Organic Materials, School of Chemistry and Chemical Engineering, Nanjing University, Nanjing, Jiangsu 210023, China*

Lei Wang − *MOE Key Laboratory of Mesoscopic Chemistry, MOE Key Laboratory of High Performance Polymer Materials and Technology, Jiangsu Key Laboratory of Advanced Organic Materials, School of Chemistry and Chemical Engineering, Nanjing University, Nanjing, Jiangsu 210023, China*

Songyuan Yang − *MOE Key Laboratory of Mesoscopic Chemistry, MOE Key Laboratory of High Performance Polymer Materials and Technology, Jiangsu Key Laboratory of Advanced Organic Materials, School of Chemistry and Chemical Engineering, Nanjing University, Nanjing, Jiangsu 210023, China*

Junchuan Liang − *MOE Key Laboratory of Mesoscopic Chemistry, MOE Key Laboratory of High Performance Polymer Materials and Technology, Jiangsu Key Laboratory of Advanced Organic Materials, School of Chemistry and Chemical Engineering, Nanjing University, Nanjing, Jiangsu 210023, China*

Zewen Zhang − *MOE Key Laboratory of Mesoscopic Chemistry, MOE Key Laboratory of High Performance Polymer Materials and Technology, Jiangsu Key Laboratory of Advanced Organic Materials, School of Chemistry and Chemical Engineering, Nanjing University, Nanjing, Jiangsu 210023, China*

Xiaoli Zhang − *School of Materials Science and Engineering, Zhengzhou University, Zhengzhou 450001, China*

Complete contact information is available at: https://pubs.acs.org/10.1021/acs.chemmater.1c00886

Author Contributions

Z.J. and M.J. conceived the idea of this study and designed the experiments. M.J. performed the sample fabrication, electrochemical measurements, and data analysis. M.J., Y.H., W.Z., L.W., S.Y., J.L., Z.Z., and X.Z. performed the material characterizations. M.J. and Z.J. wrote and revised the paper. Z.J. planned and supervised the project.

Notes

The authors declare no competing financial interest.

■ ACKNOWLEDGMENTS

This work was financially supported by the National Key Research and Development Program of China (2017YFA0208200), the Fundamental Research Funds for the Central Universities of China (0205-14380219, 0205-14913212), the Natural Science Foundation of China (22022505, 21872069), the Natural Science Foundation of Jiangsu Province (BK20180008), and the Shenzhen Fundamental Research Program of Science, Technology and Innovation Commission of Shenzhen Municipality (JCYJ20180307155007589). The authors also acknowledge the support of STEM mapping measurements by Qin Luo from the Hitachi (China) Company.

■ REFERENCES

(1) Zhu, Y. M.; Bu, L. Z.; Shao, Q.; Huang, X. Q. Subnanometer PtRh Nanowire with Alleviated Poisoning Effect and Enhanced C−C Bond Cleavage for Ethanol Oxidation Electrocatalysis. *ACS Catal.* **2019**, *9*, 6607−6612.

(2) Zhang, J. W.; Ye, J. Y.; Fan, Q. Y.; Jiang, Y. T.; Zhu, Y. F.; Li, H. Q.; Cao, Z. M.; Kuang, Q.; Cheng, J.; Zheng, J.; Xie, Z. X. Cyclic Penta-Twinned Rhodium Nanobranches as Superior Catalysts for Ethanol Electro-oxidation. *J. Am. Chem. Soc.* **2018**, *140*, 11232−11240.

(3) Rizo, R. B.; Arán-Ais, R. M.; Padgett, E.; Muller, D. A.; Lazaro, M. J.; Gullon, J. S.; Feliu, J. M.; Pastor, E.; Abrun, H. D. Pt-$Rich_{core}$/$Sn\text{-}Rich_{subsurface}$/$Pt_{skin}$ Nanocubes As Highly Active and Stable Electrocatalysts for the Ethanol Oxidation Reaction. *J. Am. Chem. Soc.* **2018**, *140*, 3791−3797.

(4) Mao, J.; Chen, W.; He, D.; Wan, J.; Pei, J.; Dong, J.; Wang, Y.; An, P.; Jin, Z.; Xing, W.; Tang, H.; Zhuang, Z.; Liang, X.; Huang, Y.; Zhou, G.; Wang, L.; Wang, D.; Li, Y. Design of Ultrathin Pt-Mo-Ni Nanowire Catalysts for Ethanol Electrooxidation. *Sci. Adv.* **2017**, *3*, No. e1603068.

(5) Huang, L.; Zhang, X.; Wang, Q.; Han, Y.; Fang, Y.; Dong, S. Shape-control of Pt-Ru nanocrystals: tuning surface structure for enhanced electrocatalytic methanol oxidation. *J. Am. Chem. Soc.* **2018**, *140*, 1142−1147.

(6) Wang, K.; Du, H. Y.; Sriphathoorat, R.; Shen, P. K. Vertex-Type Engineering of Pt−Cu−Rh Heterogeneous Nanocages for Highly

Efficient Ethanol Electrooxidation. *Adv. Mater.* **2018**, *30*, 1804074−1804081.
(7) Kowal, A.; Li, M.; Shao, M.; Sasaki, K.; Vukmirovic, M. B.; Zhang, J.; Marinkovic, N. S.; Liu, P.; Frenkel, A. I.; Adzic, R. R. Ternary Pt/Rh/SnO_2 Electrocatalysts for Oxidizing Ethanol to CO_2. *Nat. Mater.* **2009**, *8*, 325−330.
(8) Huang, W. J.; Ma, X. Y.; Wang, H.; Feng, R. F.; Zhou, J. G.; Duchesne, P. N.; Zhang, P.; Chen, F. J.; Han, N.; Zhao, F. P.; Zhou, J. H.; Cai, W. B.; Li, Y. G. Promoting Effect of $Ni(OH)_2$ on Palladium Nanocrystals Leads to Greatly Improved Operation Durability for Electrocatalytic Ethanol Oxidation in Alkaline Solution. *Adv. Mater.* **2017**, *29*, 1703057−1703064.
(9) Zhou, Y. Y.; Xie, Z. Y.; Jiang, J. X.; Wang, J.; Song, X. Y.; He, Q.; Ding, W.; Wei, Z. D. Lattice-confined Ru clusters with high CO tolerance and activity for the hydrogen oxidation reaction. *Nat. Catal.* **2020**, *3*, 454−462.
(10) Tian, X. L.; Luo, J. M.; Nan, H. X.; Zou, H. B.; Chen, R.; Shu, T.; Li, X. H.; Li, Y. W.; Song, H. Y.; Liao, S. J.; Adzic, R. R. Transition Metal Nitride Coated with Atomic Layers of Pt as a Low-Cost, Highly Stable Electrocatalyst for the Oxygen Reduction Reaction. *J. Am. Chem. Soc.* **2016**, *138*, 1575−1583.
(11) Ottakam Thotiyl, M. M.; Ravikumar, T.; Sampath, S. Platinum particles supported on titanium nitride: an efficient electrode material for the oxidation of methanol in alkaline media. *J. Mater. Chem.* **2010**, *20*, 10643−10651.
(12) Li, H. H.; Fu, Q. Q.; Xu, L.; Ma, S. Y.; Zheng, Y. R.; Liu, X. J.; Yu, S. H. Highly crystalline PtCu nanotubes with three dimensional molecular accessible and restructured surface for efficient catalysis. *Energy Environ. Sci.* **2017**, *10*, 1751−1756.
(13) Xia, B. Y.; Wu, H. B.; Li, N.; Yan, Y.; Lou, X. W.; Wang, X. One-Pot Synthesis of Pt-Co Alloy Nanowire Assemblies with Tunable Composition and Enhanced Electrocatalytic Properties. *Angew. Chem., Int. Ed.* **2015**, *54*, 3797−3801.
(14) Li, S.; Xu, H.; Xiong, Z.; Zhang, K.; Wang, C.; Yan, B.; Guo, J.; Du, Y. Monodispersed porous flowerlike PtAu nanocrystals as effective electrocatalysts for ethanol oxidation. *Appl. Surf. Sci.* **2017**, *422*, 172−178.
(15) Zhu, Y. M.; Bu, L. Z.; Shao, Q.; Huang, X. Q. Structurally Ordered Pt_3Sn Nanofibers with Highlighted Anti-Poisoning Property as Efficient Ethanol Oxidation Electrocatalysts. *ACS Catal.* **2020**, *10*, 3455−3461.
(16) Zhang, B. W.; Lai, W. H.; Sheng, T.; Qu, X. M.; Wang, Y. X.; Ren, L.; Zhang, L.; Du, Y.; Jiang, Y. X.; Sun, S. G.; Dou, S. X. Ordered platinum−bismuth intermetallic clusters with Pt-skin for a highly efficient electrochemical ethanol oxidation reaction. *J. Mater. Chem. A* **2019**, *7*, 5214−5220.
(17) Wang, Q.; Chen, S.; Li, P.; Ibraheem, S.; Li, J.; Deng, J.; Wei, Z. Surface Ru enriched structurally ordered intermetallic PtFe@PtRuFe core-shell nanostructure boosts methanol oxidation reaction catalysis. *Appl. Catal., B* **2019**, *252*, 120−127.
(18) Li, J.; Luo, Z.; Zuo, Y.; Liu, J.; Zhang, T.; Tang, P.; Arbiol, J.; Llorca, J.; Cabot, A. NiSn bimetallic nanoparticles as stable electrocatalysts for methanol oxidation reaction. *Appl. Catal., B* **2018**, *234*, 10−18.
(19) Zhang, Y. P.; Gao, F.; Wang, C. Q.; Shiraishi, Y.; Du, Y. K. Engineering Spiny PtFePd@PtFe/Pt Core@Multishell Nanowires with Enhanced Performance for Alcohol Electrooxidation. *ACS Appl. Mater. Interfaces* **2019**, *11*, 30880−30886.
(20) Sulaiman, J. E.; Zhu, S. Q.; Xing, Z. L.; Chang, Q. W.; Shao, M. H. Pt−Ni Octahedra as Electrocatalysts for the Ethanol Electro-Oxidation Reaction. *ACS Catal.* **2017**, *7*, 5134−5141.
(21) Zhang, J.; Ma, L.; Gan, M.; Fu, S.; Zhao, Y. TiN@nitrogen-doped carbon supported Pt nanoparticles as high-performance anode catalyst for methanol electro-oxidation. *J. Power Sources* **2016**, *324*, 199−207.
(22) Zhang, L.; Ding, L. X.; Chen, H.; Li, D.; Wang, S.; Wang, H. Self-Supported PtAuP Alloy Nanotube Arrays with Enhanced Activity and Stability for Methanol Electro-Oxidation. *Small* **2017**, *13*, 1604000−1604007.
(23) Rogers, C.; Perkins, W. S.; Veber, G.; Williams, T. E.; Cloke, R. R.; Fischer, F. R. Synergistic Enhancement of Electrocatalytic CO_2 Reduction with Gold Nanoparticles Embedded in Functional Graphene Nanoribbon Composite Electrodes. *J. Am. Chem. Soc.* **2017**, *139*, 4052−4061.
(24) Hu, X. L.; Lin, C. L.; Wei, L.; Hong, C. H.; Zhang, Y. F.; Zhuang, N. F. High electrocatalytic performance of graphene nanoribbon supported PtAu nanoalloy for direct ethanol fuel cell and theoretical analysis of anti-CO poisoning. *Electrochim. Acta* **2016**, *187*, 560−566.
(25) Duchesne, P. N.; Li, Z. Y.; Deming, C. P.; Fung, V.; Zhao, X.; Yuan, J.; Regier, T.; Aldalbahi, A.; Almarhoon, Z.; Chen, S.; Jiang, D.-e.; Zheng, N.; Zhang, P. Golden single-atomic-site platinum electrocatalysts. *Nat. Mater.* **2018**, *17*, 1033−1039.
(26) Zhang, Y. L.; Li, X. K.; Li, K.; Xue, B.; Zhang, C. M.; Du, C.; Wu, Z. J.; Chen, W. Novel Au Catalysis Strategy for the Synthesis of Au@Pt Core-Shell Nanoelectrocatalyst with Self-Controlled Quasi-Monolayer Pt Skin. *ACS Appl. Mater. Interfaces* **2017**, *9*, 32688−32697.
(27) Song, P.; Mei, L.-P.; Wang, A.-J.; Fang, K.-M.; Feng, J.-J. One-pot surfactant-free synthesis of porous PtAu alloyed nanoflowers with enhanced electrocatalytic activity for ethanol oxidation and oxygen reduction reactions. *Int. J. Hydrogen Energy* **2016**, *41*, 1645−1653.
(28) Ataee-Esfahani, H.; Wang, L.; Nemoto, Y.; Yamauchi, Y. Synthesis of Bimetallic Au@Pt Nanoparticles with Au Core and Nanostructured Pt Shell toward Highly Active Electrocatalysts. *Chem. Mater.* **2010**, *22*, 6310−6318.
(29) Yu, X.; Ye, S. Recent advances in activity and durability enhancement of Pt/C catalytic cathode in PEMFC Part II: Degradation mechanism and durability enhancement of carbon supported platinum catalyst. *J. Power Sources* **2007**, *172*, 145−154.
(30) Huang, M. H.; Zhang, J. S.; Wu, C. X.; Guan, L. H. Pt Nanoparticles Densely Coated on SnO_2-Covered Multiwalled Carbon Nanotubes with Excellent Electrocatalytic Activity and Stability for Methanol Oxidation. *ACS Appl. Mater. Interfaces* **2017**, *9*, 26921−26927.
(31) Sun, S.; Zhang, G.; Geng, D.; Chen, Y.; Li, R.; Cai, M.; Sun, X. A Highly Durable Platinum Nanocatalyst for Proton Exchange Membrane Fuel Cells: Multiarmed Starlike Nanowire Single Crystal. *Angew. Chem., Int. Ed.* **2011**, *50*, 422−426.
(32) Zhou, J. G.; Zhou, X. T.; Sun, X. H.; Li, R. Y.; Murphy, M.; Ding, Z. F.; Sun, X. L.; Sham, T. K. Interaction between Pt nanoparticles and carbon nanotubes-An X-ray absorption near edge structures (XANES) study. *Chem. Phys. Lett.* **2007**, *437*, 229−232.
(33) Cheng, Y.; Xu, C.; Shen, P. K.; Jiang, S. P. Effect of nitrogen-containing functionalization on the electrocatalytic activity of PtRu nanoparticles supported on carbon nanotubes for direct methanol fuel cells. *Appl. Catal., B* **2014**, *158−159*, 140−149.
(34) Zhou, W. J.; Li, M.; Zhang, L.; Chan, S. H. Supported PtAu catalysts with different nano-structures for ethanol electrooxidation. *Electrochim. Acta* **2014**, *123*, 233−239.
(35) Feng, L.; Li, K.; Chang, J.; Liu, C.; Xing, W. Nanostructured PtRu/C catalyst promoted by CoP as an efficient and robust anode catalyst in direct methanol fuel cells. *Nano Energy* **2015**, *15*, 462−469.
(36) Huang, H.; Ma, L.; Tiwary, C. S.; Jiang, Q.; Yin, K.; Zhou, W.; Ajayan, P. M. Worm-Shape Pt Nanocrystals Grown on Nitrogen-Doped Low-Defect Graphene Sheets: Highly Efficient Electrocatalysts for Methanol Oxidation Reaction. *Small* **2017**, *13*, 1603013−1603020.
(37) Jiang, M.; Li, X.; Huang, W.; Gan, M.; Hu, L.; He, H.; Zhang, H.; Xie, F.; Ma, L. Fe_2O_3@FeP core-shell nanocubes/C composites supported irregular PtP nanocrystals for enhanced catalytic methanol oxidation. *Electrochim. Acta* **2019**, *323*, No. 134813.
(38) Wang, K. L.; Wang, H.; Pasupathi, S.; Linkov, V.; Ji, S.; Wang, R. F. Palygorskite promoted PtSn/carbon catalysts and their intrinsic catalytic activity for ethanol oxidation. *Electrochim. Acta* **2012**, *70*, 394−401.
(39) Jiang, M. H.; Ma, L.; Gan, M. Y.; Hu, L. Q.; He, H. M.; Xie, F.; Zhang, H. H. Worm-like PtP nanocrystals supported on $NiCo_2P_x$/C

https://doi.org/10.1021/acs.chemmater.1c00886
Chem. Mater. 2021, 33, 3767−3778

composites for enhanced methanol electrooxidation performance. *Electrochim. Acta* **2019**, *293*, 30−39.
(40) Zhang, J.; Ji, Y. J.; Wang, P. T.; Shao, Q.; Li, Y. Y.; Huang, X. Q. Adsorbing and Activating N_2 on Heterogeneous Au−Fe_3O_4 Nanoparticles for N_2 Fixation. *Adv. Funct. Mater.* **2020**, *30*, 1906579−1906586.
(41) Zhang, Y. P.; Gao, F.; Wang, C. Q.; Shiraishi, Y.; Du, Y. K. Engineering Spiny PtFePd@PtFe/Pt Core@Multishell Nanowires with Enhanced Performance for Alcohol Electrooxidation. *ACS Appl. Mater. Interfaces* **2019**, *11*, 30880−30886.
(42) Mayilvel Dinesh, M.; Huang, T.; Yao, S.; Sun, G.; Mao, S. Hafnium sulphide-carbon nanotube composite as Pt support and active site-enriched catalyst for high performance methanol and ethanol oxidations in alkaline electrolytes. *J. Power Sources* **2019**, *410−411*, 204−212.
(43) Lv, H.; Sun, L.; Xu, D.; Ma, Y.; Liu, B. When ternary PdCuP alloys meet ultrathin nanowires: Synergic boosting of catalytic performance in ethanol electrooxidation. *Appl. Catal., B* **2019**, *253*, 271−277.
(44) Wu, T.; Fan, J. C.; Li, Q. X.; Shi, P. H.; Xu, Q. J.; Min, Y. L. Palladium Nanoparticles Anchored on Anatase Titanium Dioxide-Black Phosphorus Hybrids with Heterointerfaces: Highly Electroactive and Durable Catalysts for Ethanol Electrooxidation. *Adv. Energy Mater.* **2018**, *8*, 1701799−1701809.
(45) Yu, X. T.; Luo, Z. S.; Zhang, T.; Tang, P. Y.; Li, J. S.; Wang, X.; Llorca, J.; Arbiol, J.; Liu, J. F.; Cabot, A. Stability of Pd_3Pb Nanocubes during Electrocatalytic Ethanol Oxidation. *Chem. Mater.* **2020**, *32*, 2044−2052.
(46) Tsang, C. H. A.; Hui, K. N.; Hui, K. S. Influence of Pd_1Pt_x alloy NPs on graphene aerogel/nickel foam as binder-free anodic electrode for electrocatalytic ethanol oxidation reaction. *J. Power Sources* **2019**, *413*, 98−106.
(47) Chen, Y. J.; Chen, Y. R.; Chiang, C. H.; Tung, K. L.; Yehc, T. K.; Tuan, H. Y. Monodisperse ordered indium-palladium nanoparticles: synthesis and role of indium for boosting superior electrocatalytic activity for ethanol oxidation reaction. *Nanoscale* **2019**, *11*, 3336−3343.
(48) Wei, M.; Zhang, L. L.; Luo, D.; Ding, L. X.; Wang, S. Q.; Wang, H. H. Graphene-assisted synthesis of PdFe-embedded porous carbon nanofibers for efficient ethanol electrooxidation. *Electrochim. Acta* **2018**, *289*, 311−318.
(49) Zhang, J. W.; Ye, J. Y.; Fan, Q. Y.; Jiang, Y. T.; Zhu, Y. F.; Li, H. Q.; Cao, Z. M.; Kuang, Q.; Cheng, J.; Zheng, J.; Xie, Z. X. Cyclic Penta-Twinned Rhodium Nanobranches as Superior Catalysts for Ethanol Electro-oxidation. *J. Am. Chem. Soc.* **2018**, *140*, 11232−11240.
(50) Chen, L.; Lu, L.; Zhu, H.; Chen, Y.; Huang, Y.; Li, Y.; Wang, L. Improved ethanol electrooxidation performance by shortening Pd−Ni active site distance in Pd−Ni−P nanocatalysts. *Nat. Commun.* **2017**, *8*, No. 14136.
(51) Wang, Q.; Chen, S.; Li, P.; Ibraheem, S.; Li, J.; Deng, J.; Wei, Z. Surface Ru enriched structurally ordered intermetallic PtFe@PtRuFe core-shell nanostructure boosts methanol oxidation reaction catalysis. *Appl. Catal., B* **2019**, *252*, 120−127.
(52) Tian, H.; Li, Z.; Feng, G.; Yang, Z.; Fox, D.; Wang, M.; Zhou, H.; Zhai, L.; Kushima, A.; Du, Y.; Feng, Z.; Shan, X.; Yang, Y. Stable, high-performance, dendrite-free, seawater-based aqueous batteries. *Nat. Commun.* **2021**, *12*, No. 237.
(53) Wang, G.; Aubin, M.; Mehta, A.; Tian, H.; Chang, J.; Kushima, A.; Sohn, Y.; Yang, Y. Stabilization of Sn Anode through Structural Reconstruction of a Cu−Sn Intermetallic Coating Layer. *Adv. Mater.* **2020**, *32*, 2003684−2003692.

https://doi.org/10.1021/acs.chemmater.1c00886
Chem. Mater. 2021, 33, 3767−3778